Research Article | Vol. 31, No. 13 / 19 Jun 2023 / Optics Express 20836
Optics EXPRESS

Full-Stokes parameters detection enabled by a non-interleaved fiber-compatible metasurface

JIAQI QU,[1] ZHUO WANG,[2] ZHI CEHNG,[1] YUE WANG,[1] AND CHANGYUAN YU[1,3,*]

[1]Photonics Research Institute, Department of Electronic and Information Engineering, The Hong Kong Polytechnic University, Kowloon, Hong Kong
[2]Photonics Research Institute, Department of Electrical Engineering, The Hong Kong Polytechnic University, Kowloon, Hong Kong
[3]The Hong Kong Polytechnic University Shenzhen Research Institute, Shenzhen 518057, China
*changyuan.yu@polyu.edu.hk

Abstract: Polarization of the optical field determines the way of light-matter interaction, which lays the foundation for various applications such as chiral spectroscopy, biomedical imaging, and machine vision. Currently, with the rise of the metasurface, miniaturized polarization detectors have attracted extensive interest. However, due to the limitation of the working area, it is still a challenge to integrate polarization detectors on the fiber end face. Here, we propose a design of compact non-interleaved metasurface that can be integrated on the tip of a large-mode-area photonic crystal fiber (LMA-PCF) to realize full-Stokes parameters detection. Through concurrent control over the dynamic phase and Pancharatnam-Berry (PB) phase, different helical phases are assigned to the two orthogonal circular polarization bases, of which the amplitude contrast and relative phase difference can be represented by two non-overlapped foci and an interference ring pattern, respectively. Therefore, the determination of arbitrary polarization states through the proposed ultracompact fiber-compatible metasurface can be achieved. Moreover, we calculated full-Stokes parameters according to simulation results and obtained that the average detection deviation is relatively low at 2.84% for 20 elucidated samples. The novel metasurface exhibits excellent polarization detection performance and overcomes the limitation of the small integrated area, which provides insights into the further practical explorations of ultracompact polarization detection devices.

1. Introduction

Composed of subwavelength atoms with artificially designed geometric parameters, the metasurface exhibits the profound capability to manipulate lightwave with a full degree of freedom such as phase, amplitude, spectral response, and polarization [1,2]. The ultrathin and highly compact natures of metasurface have boosted versatile integrations of meta devices with many conventional optical systems like metalens-based endoscopes [3], nanoscale vortex lasers [4] and optofluidic refractive index sensing system [5]. In particular, metasurface integrated with optical fiber has attracted a burgeoning amount of interest inspired by the emerging scheme "lab-on fiber". Flat nanostructures can be patterned on the facets (the end face of the fiber core and the side face of the D-shaped fiber) of the optical fiber and have strong interactions with the guided light [6]. Multiple initial attempts to fabricate nanostructures on fiber-tip have sprung up in recent years, with potential applications ranging from beam focusing [7–9], beam splitter [10], vortex beam generator [11], and biosensing [12]. These fiber-tip meta-devices are easy-integrable in optical systems and possess more advanced functionalities compared to conventional fiber devices. More importantly, the rigorous alignment process can be omitted with the fiber-tip meta-devices equipped. Prior research has thoroughly investigated phase [7–13] and

#491836 https://doi.org/10.1364/OE.491836
Journal © 2023 Received 4 Apr 2023; revised 6 May 2023; accepted 20 May 2023; published 6 Jun 2023

Optics EXPRESS

amplitude [13] modulation of the output light coming from the end face of the fiber. However, polarization-related research based on fiber-tip metasurface was rarely explored.

Highly integrated modern optical systems provide the demand for miniaturized polarization detectors. However, limited by the current photodetectors that exclusively respond to light intensity, conventional polarization measurements require a series of cascaded components like wave plates, polarizers, and mechanically rotating devices [14], which severely impede the integration and miniaturization trends of optical systems. In pursuit of extremely compact size, great efforts have been made to the metasurface-enabled polarization detection devices. The proposed meta-devices aim to accomplish partial or complete retrieval of the Stokes parameters [15], which are one of the most commonly used representations of the state of polarization (SOP). Compared to the complete retrieval of the Stokes parameters, partial retrieval is much easier due to its monotonous function and thus leading to a smaller required working area for the metasurface arrangement. Among the investigations on partial retrieval, orientation angle detection for linearly polarized (LP) light [16] and ellipticity detection for elliptically polarized (EP) light [17,18] have been widely explored. The simultaneous operation of the two detections has also been studied thoroughly using helical phase modulation [19]. As for complete retrieval of the Stokes parameters, the sectional unit cell (UC) pattern scheme is initially put forward using dielectric [20] or plasmonic nanostructures [21–23]. The designed metasurfaces incorporate separate sections, with each section functioning as distinct detection of the Stokes parameters, leading to an intuitive representation of SOP. However, the space division scheme inevitably results in low efficiency of the whole device. Apart from the sectional pattern scheme, interleaved UC pattern scheme has been proposed by means of spatially splitting the orthogonal polarizations [24] or enabling interference between generated images through different series of UCs [25]. The interleaved pattern scheme shares the same defect as the sectional pattern scheme. In other words, it is necessary for the designs to have a large area for UC arrangement, otherwise, the integration with a compact platform like an optical fiber core is impractical. Non-interleaved method, which requires a smaller size of metasurface pattern area, has gradually been proposed to address the aforementioned issue. Polarization-selective directional scattering enabled polarimeter is proposed for full-Stokes parameter detection, though the non-interleaved rod antennas are not closely spaced [26]. A non-interleaved meta-device [27] is designed regarding the matrix Fourier transform for full-Stokes polarization representation, while the number of distinguishable polarization states is limited due to the indispensably precoded hologram of each state. Another design based on non-interleaved UC can arbitrarily detect SOP [28], but the specific resonant phase selection of UC results in a low transmission efficiency of 63.7%, which dramatically reduces the operation efficiency.

Herein, we propose a novel approach to efficiently achieve full-Stokes parameters measurement using the compact non-interleaved metasurface integrated on the tip of a large-mode-area photonic crystal fiber (LMA-PCF). A series of dielectric nano bricks with a high transmission and conversion efficiency of over 90% are arranged in a non-interleaved sequence for concurrent control of the dynamic phase and Pancharatnam Berry (PB) phase. In addition, the metasurface is engineered to add helical phase modulations with topological charges of $+1$ and -1 onto the left-handed polarized (LCP) and right-handed polarized (RCP) components of the incident light, respectively. Then, the transmission light will generate two non-overlapped foci and an overlapped interference ring pattern. Considering the orthogonal basis formed by LCP and RCP light, the chiral phase difference can be obtained from the dark fringe direction of the interference ring pattern, and the chiral amplitude contrast can be obtained through intensity comparison between the non-overlapped foci, which can be used for the deduction of full-Stokes parameters. Hence, arbitrary polarization states, as well as the full-Stokes parameters, can be obtained with the proposed ultracompact fiber-compatible metasurface. Simulation results demonstrate a good performance of Stokes parameters detection with a low detection deviation

Optics EXPRESS

rate of 2.84% among 20 incident samples. Our design is featured a compact footprint and excellent detection performance, which is expected to unlock the full potential of optical fiber-compatible meta-devices and leverage its practical functionality in photonic systems.

2. Theory and method

2.1. Principle of polarization measurement

It is commonly known that arbitrarily polarized light is considered as the superposition of LCP and RCP components. Thus, any fixed polarization can be described by the chiral phase difference and chiral amplitude contrast. The working scheme of our design relies on the detection of the chiral phase difference and chiral amplitude contrast of the incident light through joint control over the dynamic phase and PB phase. We assign different phase profiles for LCP and RCP components and the designed patterns generated by LCP and RCP contain a ring-shaped pattern and a focus inside the ring. Helical phases with topological charges of +1 and −1 are precisely engineered to the ring patterns of LCP and RCP components, respectively, leading to an interference accompanied with the dark fringe region. Meanwhile, orthogonal circularly polarized light components are designed to focus in opposite directions at the display plane. The merged pattern for arbitrarily polarized light is shown in Fig. 1(a). The ring pattern is responsible for chiral phase difference assessment and the foci pattern is for chiral amplitude contrast determination. m and n are integers that digitally describe the proportion of circular orthogonal bases of the incidence.

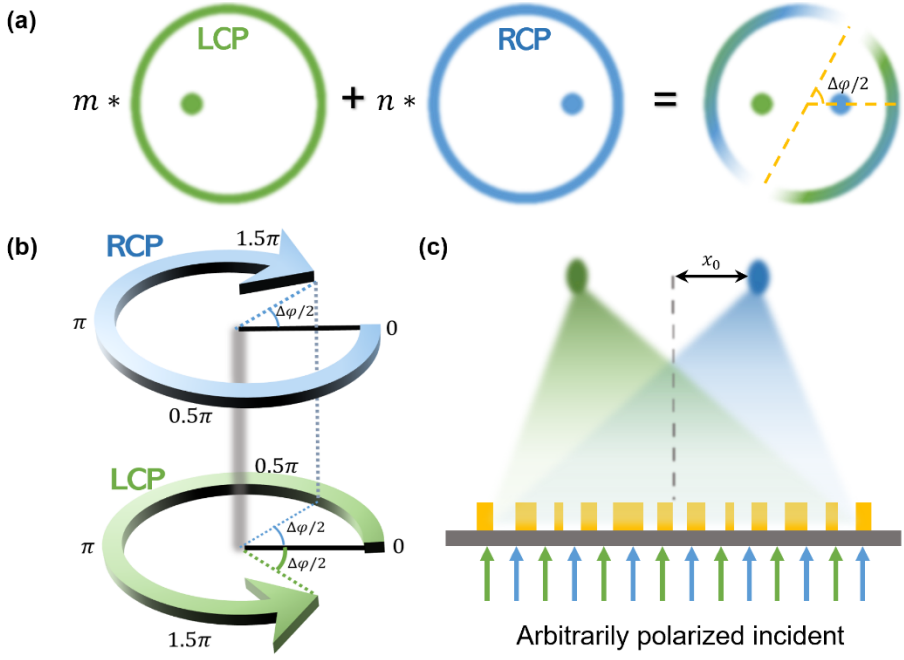

Fig. 1. Working scheme of the proposed design. (a) Generated LCP and RCP images with an overlapped ring and foci in separate positions (left or right) under the illumination of RCP and LCP lights, respectively. (b) Illustration of the initial chiral phase difference $\Delta\varphi$ between RCP and LCP components. The zero-phase point is located at the orientation angle $\Delta\varphi/2$. (c) Side view of the left and right foci generated from RCP and LCP under arbitrarily polarized light.

Optics EXPRESS

During the chiral phase difference assessment, the key point is the interference between two generated ring-shaped patterns enabled by RCP and LCP components. It is commonly known that RCP and LCP light can be represented in terms of LP components: $\vec{l} = \frac{\sqrt{2}}{2}\begin{bmatrix} 1 \\ -i \end{bmatrix}$ and $\vec{r} = \frac{\sqrt{2}}{2}\begin{bmatrix} 1 \\ i \end{bmatrix}$. Upon illumination of arbitrarily polarized light, the polarization typically follows,

$$\vec{P} = a_l e^{i\varphi_l}\vec{l} + a_r e^{i\varphi_r}\vec{r} \tag{1}$$

where a_l and a_r are the amplitudes of the LCP and RCP components, respectively. φ_l and φ_r express the phases of LCP and RCP lights, respectively. We assume $\Delta\varphi$ is the initial phase difference between LCP and RCP, namely $\Delta\varphi = \varphi_l - \varphi_r$. Thus, the phase difference between the zero-phase angle and the two components are both $\Delta\varphi/2$, and the zero-phase angle along the ring represents the polarization orientation angle, which is illustrated in Fig. 1(b). To enable the interference between two CP components, the additional helical phases with topological charges of +1 and −1 are introduced for LCP and RCP incident lights, respectively. Since the PB phase converts the circular handedness of the light, the generated RCP and LCP components obtain +1 and −1 topological charges accordingly. The phase distributions of ring-shaped patterns for RCP and LCP incidents are shown below,

$$\varphi_{r_{L/R}}(r) = -\frac{2\pi}{\lambda}\left(\sqrt{r^2 + f^2} - f\right) \pm \arctan\left(\frac{y}{x}\right) \tag{2}$$

where r is the ring radius corresponding to the center of the proposed device, and f is the distance between the display plane and the meta-device (f is designed as 20 um). λ is the operation wavelength and here we utilized the common communication wavelength 1310 nm. Due to the introduced helical phase, an arbitrary point along the ring with an orientation angle of θ exhibits a helical phase difference between LCP and RCP of 2θ. We assume $\varphi_R(\theta)$ and $\varphi_L(\theta)$ are the helical phases of RCP and LCP along the ring, and $\varphi_R(\theta) - \varphi_L(\theta) = 2\theta$. Hence, the distribution of the generated ring-shaped pattern after light transmitting through the device can be explicated as,

$$\overrightarrow{P_{ring}}(\theta) = a_l e^{i(\varphi_l + \varphi_R(\theta))}\vec{r} + a_r e^{i(\varphi_r + \varphi_L(\theta))}\vec{l} = e^{i(\varphi_r + \varphi_L(\theta))}\{a_l e^{i(\Delta\varphi - 2\theta)}\vec{r} + a_r\vec{l}\} \tag{3}$$

We notice that the distribution is the function of θ. Correspondingly, the intensity profiles along the ring with respect to the x- and y-component are expressed as,

$$\begin{cases} I_x = \frac{1}{2}{a_l}^2 + \frac{1}{2}{a_r}^2 + a_l a_r \cos(2\theta - \Delta\varphi) \\ I_y = \frac{1}{2}{a_l}^2 + \frac{1}{2}{a_r}^2 - a_l a_r \cos(2\theta - \Delta\varphi) \end{cases} \tag{4}$$

It is clear that the intensity profiles of the x-direction and y-direction are both the function of θ, and vary between minimal and maximal values alternatively while θ ranges from 0 to 2π. In this case, the chiral phase difference $\Delta\varphi$ can be estimated with the x- or y-component intensity measured along the ring. In the following simulations and discussions, we will apply the y-component intensity for polarization detection.

On the subject of chiral amplitude contrast determination, the phase profiles for LCP and RCP components to facilitate the foci are shown below,

$$\varphi_{f_{L/R}}(x, y) = -\frac{2\pi}{\lambda}\left(\sqrt{(x \pm x_0)^2 + y^2 + f^2} - \sqrt{f^2 + {x_0}^2}\right) \tag{5}$$

where x_0 represents the distance between the foci and the center of the display pattern (here x_0 is 4 um) and f is the designed focal length. Based on the phase profiles specifically designed for LCP

Optics EXPRESS

and RCP incident lights, two foci located at the left and right sides are precisely enabled, which is illustrated in Fig. 1(c). Since arbitrary polarized illumination is considered as the superposition of the LCP and RCP components, different ratio of the intensity of two foci represents different chiral amplitude contrast. The intensities of two foci are derived within the integrated region with the side width set to three times the full width at half maximum (FWHM).

2.2. Stokes parameters characterization

The Stokes vector formalism has been considered as one of the most direct and commonly used ways to represent the polarization of light. There are four parameters contained in Stokes parameters: $\boldsymbol{S} = [S_0, S_1, S_2, S_3]$. For the fully polarized light, the Stokes parameters are indicated in the following equations,

$$\begin{cases} S_0 = I \\ S_1 = (I_{0^\circ} - I_{90^\circ})/I \\ S_2 = (I_{45^\circ} - I_{-45^\circ})/I \\ S_3 = (I_{RCP} - I_{LCP})/I \end{cases} \tag{6}$$

I is the overall intensity of the incident. For fully polarized light, I equals the addition of I_{RCP} and I_{LCP}. Besides, I_{0°, I_{90°, I_{45°, I_{-45° represent the intensity along 0°, 90°, 45°, −45° direction in the linear polarization bases and I_{RCP}, I_{LCP} are the intensity of RCP light and LCP light. To note, $[S_1, S_2, S_3]$ represented here have been normalized to S_0 for the fully polarized light. Under this representation, a series of cascaded optical intensity measurement components are needed inevitably for the extraction of Stokes parameters in the traditional detection method.

In our design, the polarization characteristic process is surprisingly simplified. The initial step starts with the determination of S_3. As discussed in Section 2.1, LCP and RCP results in separate foci within the ring pattern. Followed by Eq. (6), the value of S_3 is determined by the integrated optical intensity over the left and right foci. Subsequently, the tangent plane formed by S_3 latitude (shown in Fig. 2) combined with chiral phase difference $\Delta\varphi$ obtained before, will contribute to the calculation of S_1 and S_2, which can be expressed as,

$$\begin{cases} S_1 = \sqrt{1 - {S_3}^2}\cos\Delta\varphi \\ S_2 = \sqrt{1 - {S_3}^2}\sin\Delta\varphi \end{cases} \tag{7}$$

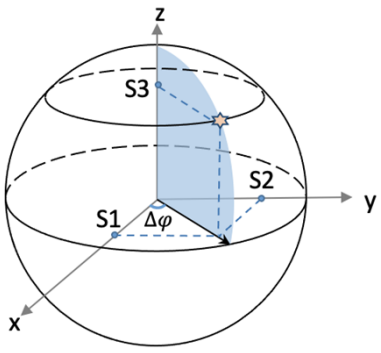

Fig. 2. State of polarization concerning the Stokes parameters and chiral phase difference $\Delta\varphi$ on the Poincare sphere.

To summarize, the Stokes parameters can be calculated through the comparison of the intensity of two foci and the assessment of the chiral phase difference. Accordingly, the obtained Stokes

Optics EXPRESS

parameters will be compared with the theoretical values of the incident light. The detail of the calculation of theoretical parameters derived from the general expression of the incident is shown in Appendix A. The detection deviation rate e is defined as the ratio of the deviation to the total measurement range. Since the Stokes parameters cover the range from −1 to 1, the total measurement range is calculated as 2.

$$e = (S_d - S_t)/2 \tag{8}$$

where S_d is the detected Stokes parameter according to the simulation results and S_t is the theoretical parameter of the incident light. The formula is applicable for all the Stokes parameters.

2.3. Unit cells selection

The size and shape of nano bricks affect the propagation phase of the transmitted light. Figures 3(a) and 3(b) depict the schematic illustration of a single UC with a uniform height of H = 800 nm (≈0.61λ), and the period is given by P = 600 nm. The nano brick patterned on the silicon dioxide (SiO_2) substrate is made of Amorphous Silicon (a-Si), providing a high refractive index of 3.496 operating at λ=1310 nm (detailed information on the refractive index of the fabricated a-Si based on practical fabrication process is shown in Table 1 in Appendix B). The widths of UC (L and W) are aligned parallel to the x-axis and y-axis, respectively. With regard to the geometry of the UC, propagation phase shift and transmission of the eight selected unit cells for an x-polarized plane wave are signified in Fig. 3(c) with the assistance of a finite-difference time-domain (FDTD) tool. While maintaining sufficiently high transmission, the set of eight UCs whose propagation phase shift covers the entire 2π phase span should be properly chosen. In addition to the propagation phase modulation, the PB phase modulation is also utilized in the device. Thus, each UC is designed to work as a half-wave plate for polarization conversion. Each UC exhibits a relatively high polarization conversion efficiency (PCE) at the operation wavelength, which are shown in Fig. 3(d-k).

2.4. Non-interleaved pattern scheme on the fiber-tip

Different from spatially dividing metasurface for distinct functions, our scheme exploits the non-interleaved arrangement of the selected UCs. The phase distributions for LCP and RCP-generated ring and focus patterns are discussed in Section 2. In our design, ring and focus patterns are combined by the holographic principle shown in Eq. (9). In this way, only one set of UCs can accomplish two functions, which significantly reduces the required pattern area for the metasurface and makes it possible to be integrated on the fiber tip. The phase profiles for LCP and RCP are elucidated below,

$$\begin{cases} \varphi_L = \mathrm{ang}(e^{i(a*\varphi_{f_L} + b*\varphi_{r_L})}) \\ \varphi_R = \mathrm{ang}(e^{i(a*\varphi_{f_R} + b*\varphi_{r_R})}) \end{cases} \tag{9}$$

where a and b are integers and the ratio of a and b is the proportion of the generated focus with the ring-shaped pattern. Based on the results of simulations, we choose the value of the ratio as 0.5 for a clear illustration of the generated pattern. In this design, joint control over the dynamic phase and PB phase is adopted to fulfill the phase profiles for orthogonal circular bases. Thus, the propagation phase $\phi(x, y)$ and PB phase required rotation angle $\theta(x, y)$ theoretically follows,

$$\begin{cases} \phi(x,y) = \frac{1}{2}[(\varphi_L(x,y) - 2n_1\pi) + (\varphi_R(x,y) - 2n_2\pi)] \\ \theta(x,y) = \frac{1}{4}[(\varphi_L(x,y) - 2n_1\pi) - (\varphi_R(x,y) - 2n_2\pi)] \end{cases} \tag{10}$$

where n_1 and n_2 are integers to ensure the obtained phase distributions are within $0 - 2\pi$ range. The proper UC at the specific location with respect to the required propagation phase shift and rotation angle will be arranged; thus, arbitrary dual-phase modulation can be achieved.

Optics EXPRESS

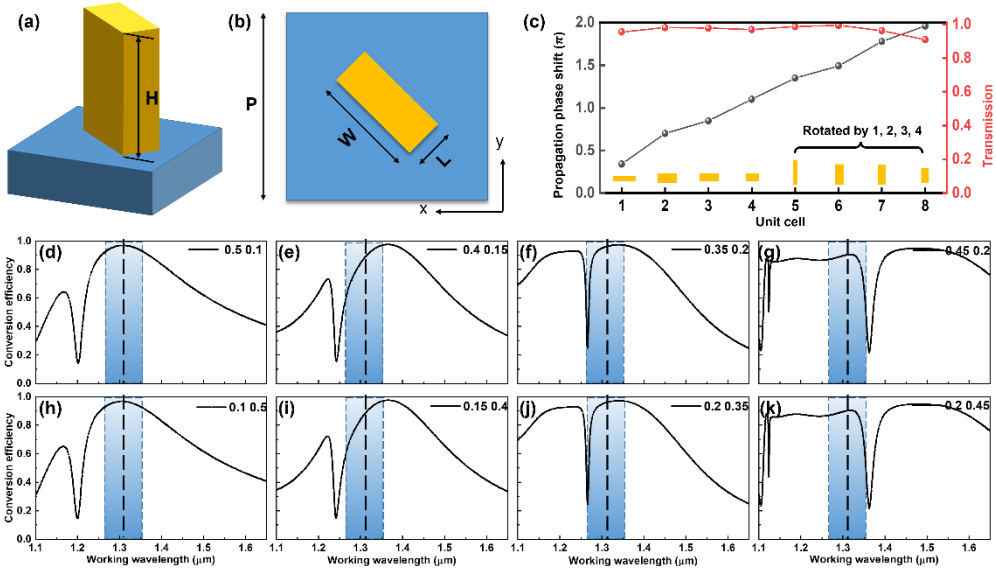

Fig. 3. (a), (b) Schematic illustration of the metalens unit cell, which is composed of nano bricks with a height of 800 nm and period of 600 nm. (c) Simulated propagation phase shift and transmission of eight selected unit cells with the x-polarized incident. The size (L and W) of the selected unit cells from 1 to 8 are L = 500, 400, 350, 450, 100, 150, 200, and 200 nm, and W = 100, 150, 200, 200, 500, 400, 350, and 450 nm. (d)-(k) The polarization conversion efficiency of the selected unit cells (from 1–8).

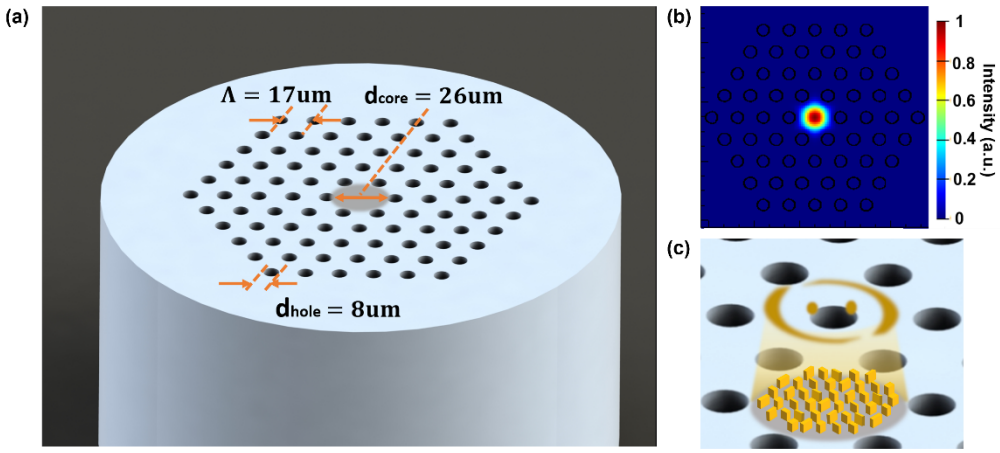

Fig. 4. (a) Illustration of LMA-PCF with the designed metasurface patterned within the core area (in grey). (b) Simulated fundamental mode profile of LMA-PCF operating at 1310 nm. (c) Detailed schematic demonstration of the proposed design for generation of the ring pattern and two off-axis foci.

The schematic illustration of the fiber-tip device is signified in Fig. 4, and here we employ the LMA-PCF as the platform to integrate the designed meta-device for its relatively large core area. Endless single-mode property in a broad operating wavelength range is maintained in the pure silica fiber core with a diameter of 26 um, while the period (Λ) and diameter of the air hole (d_{core}) are 17 um and 8 um, respectively. The simulated fundamental mode profile of the LMA-PCF is

Optics EXPRESS

shown in Fig. 4(b), which substantiates the well-confined single-mode transmitted light within the core region. The electric field component of the fundamental mode in the LMA-PCF is recorded and considered as the guided mode to serve as the source in the simulation. Thus, the total pattern area for the metasurface is the fiber core with the diameter of 26 um. The potential fabrication process is expressed in Appendix C.

3. Results and discussion

3.1. Polarization characterization process

In this section, we will introduce the basic characterization process of polarization. Taking the 135° LP incidence as an example, the normalized y-component intensity of the generated image is shown in Fig. 5. The azimuth angle θ of the polarization can be intuitively observed from the orientation of the dark fringe of interference. According to the previous discussion, the y-component intensity along the ring demonstrates a sinusoidal curve (black solid line) in Fig. 5(b). Curve fitting was conducted to the ring intensity for extraction of the parameters in a simplified version of Eq. (4), which is $I = (1 - \cos(2\theta - \Delta\varphi))/2$. For this case, $\Delta\varphi$ is fitted with -0.5524π and the sinusoidal function is specified in the green line. The R-square value of the fitness is up to 0.9381, which suggests a good performance of curve fitting. Compared to the ideal intensity along the ring (in red line), the fitting data (in green line) are reliable with little deviation. From the fitted data of ring intensity, the chiral phase difference can be obtained.

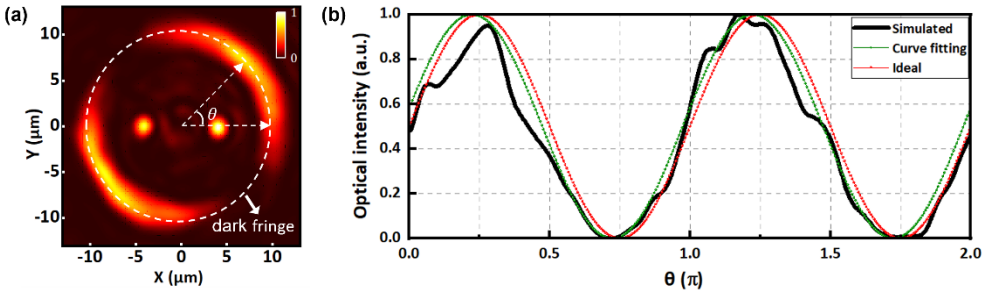

Fig. 5. (a) Optical intensity of y-component light at the display plane with the illumination of 135° LP light. The inset white arrow points to the maximum intensity. (b) Normalized intensity distributions along the ring as the function of azimuth angle θ.

Subsequently, chiral amplitude contrast as well as S_3 are available according to Eq. (6) concerning the integrated intensity over the fixed square area over the designed foci. The side width of the square is set to three times the FWHM of the focus. It is worth noting that the background noise is eliminated in the integrated intensity to enhance the accuracy of S_3 assessment.

3.2. Performance of orientation angle and chiral amplitude contrast detection

As previously described, the generated image originated from the designed metasurface is spatially divided into two parts, namely the circular ring part and the focus part. The circular ring part determines the orientation angle assessment and the focus part determines the chiral amplitude contrast calculation. In this section, two functions are tested to characterize the performance of the proposed fiber-tip meta-device. Two simple cases are taken into account, the first case is LP incident lights with different polarization orientations, and the second case is EP lights consisting of x- and y-component of equal intensity but with different phase differences σ (expressions can be found in Appendix A Eq. (11)). The comparations of simulated results and theoretical results are shown in Fig. 6.

Optics EXPRESS

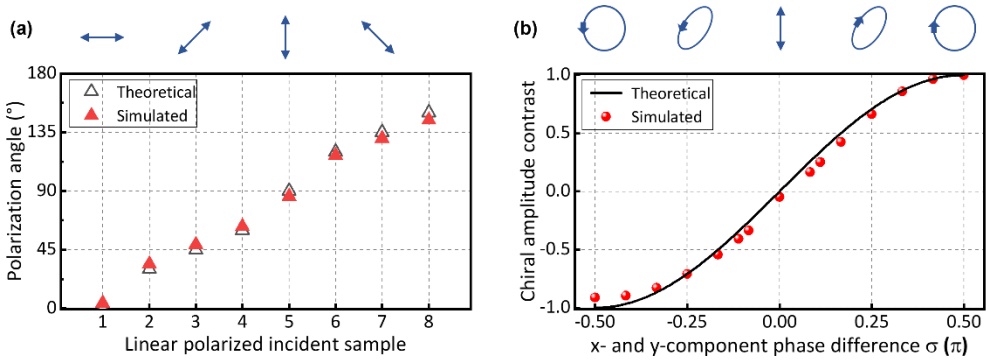

Fig. 6. (a) Theoretical (black and hollow triangle) and simulated (red and solid triangle) orientation angles of different LP light. (b) Relationship between x- and y-component phase difference σ and chiral amplitude contrast with theoretical and simulated results.

It can be observed that the simulated value (red solid triangle) indicates a good agreement with the theoretical value (black hollow triangle). The detection deviation rate is defined as the ratio of the deviation to the total measurement range. As shown in Fig. 6(a), the incident lights with LP orientations varying from 0° to 150° are analyzed. Since 180° LP light exhibits the same with 0°, the result is eliminated here. The derived average deviation rate is 1.11% within the eight samples. For the case of EP illumination, the phase difference σ between the x- and y-component varies from -0.5π to 0.5π while the ratio of the amplitude of the two components remains 1:1 for the whole test as illustrated in Fig. 6(b). The obtained simulation results (in red dots) suggest a slight derivation from the theoretical curve and the obtained deviation rate is 2.46%. To summarize, the performance of orientation angle detection and ellipticity assessment shows good reliability and high consistency.

3.3. *Full-Stokes parameters detection for arbitrarily polarized light*

To further evaluate the practicality of the device, we apply arbitrarily polarized light as the incident for general extraction of the Stokes parameters. Here, we randomly select four incident lights with different SOP as the input and collect the y-component optical intensity at the display plane, which are shown in the upper row of Fig. 7. For an intuitive illustration of the polarization states of the four incidents, the polar plots and polarization ellipse representations are summarized based on the obtained Stokes parameters and shown in the figure. It is clear that simulated results (specified in the red line) exhibit high consistency with the corresponding ideal results (specified in the black line). The handedness of the incident is also available according to the calculated Stokes parameters and is labeled in the yellow arrow in the figure.

We further add up to 20 samples to verify the stability of the full Stokes parameters detection. As illustrated in Fig. 8, simulation results in red solid circles match well with the theoretical values in blue circles among all the sample incident lights. To note, since the randomly selected inputs all belong to fully polarized light, S_1, S_2, and S_3 are normalized to the overall light intensity S_0. We calculated the deviation rate according to Eq. (8), and the detailed data are available in Table 2 in Appendix D. The obtained average deviation rate of S_1, S_2, and S_3 are 3.84%, 2.48% and 2.20%, respectively. Thus, the overall detection deviation can be calculated as 2.84%.

Optics EXPRESS

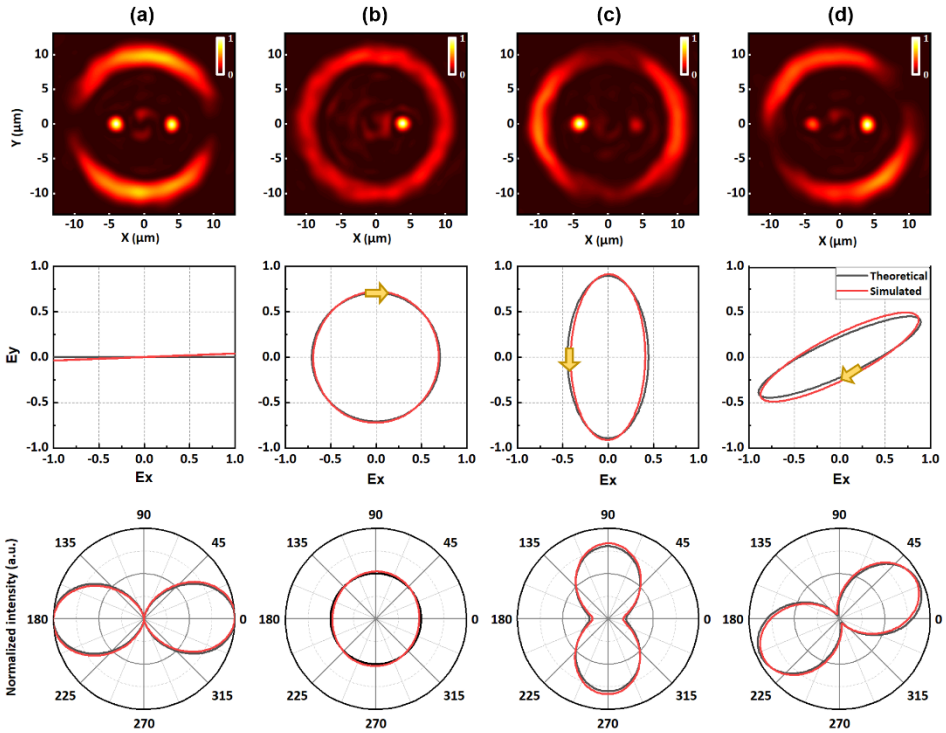

Fig. 7. Simulation results of four incident lights with different SOP. The upper row: Normalized optical intensities of y-component at the display plane. Polar plots (center row) and polarization ellipse expressions (lower row) are analyzed based on the obtained Stokes parameters. Theoretical values are shown in black lines and simulated values are shown in red lines.

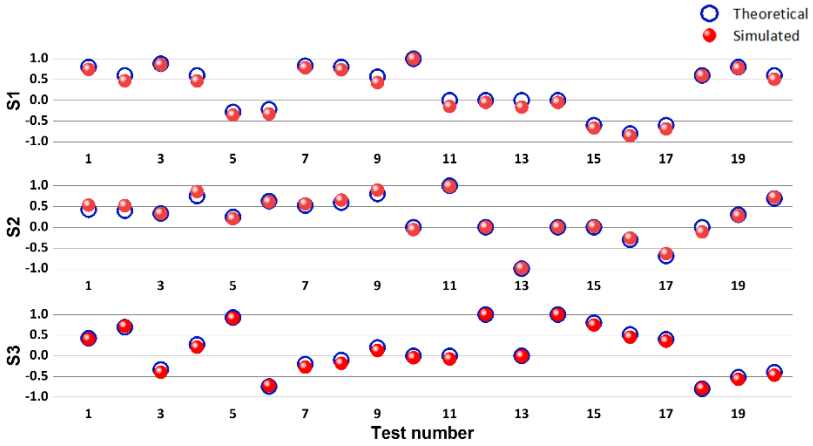

Fig. 8. Comparison of the measured Stokes parameters (red solid circles) of 20 incident samples with the theoretical values (blue circles).

Optics EXPRESS

4. Conclusions

To summarize, the proposed design based on the non-interleaved UC pattern scheme possess the capability to detect the full-Stokes parameters within the small fiber core region. Overlapped ring-shaped patterns and non-overlapped foci parts in the generated image are utilized to resolve the chiral phase difference and chiral amplitude contrast of the incident. The average detection deviations of orientation angles of LP light and ellipticities of specified EP light are 1.1% and 2.5%, respectively. For arbitrarily polarized light, the full-Stokes parameters are obtained with average detection deviations of 3.84%, 2.48%, and 2.20% on S_1, S_2, and S_3 parameters. The results suggest that the designed fiber-tip metasurface accomplishes full-Stokes parameters detection with a relatively low detection deviation rate and tackles the limitation of the small pattern area. This study establishes a quantitative framework for detecting polarization in fiber-compatible environments, which is believed to be a fruitful area for miniaturized polarization detection research.

Appendix

A. Theoretical Stokes parameter from the general expression of the incident light

Here, we will introduce another description of Stokes parameters under the general expression of the lightwave oscillates. The lightwave oscillate is typically described in orthogonal basis x- and y-direction,

$$\begin{cases} E_x = a_1 \cos \tau \\ E_y = a_2 \cos(\tau + \sigma) \end{cases} \tag{11}$$

where a_1 and a_2 are the amplitudes of the x- and y-component and σ represents the phase difference between the two components. Accordingly, the Stokes parameter can be described as the function of a_1, a_2 and σ,

$$\begin{cases} S_1 = {a_1}^2 - {a_2}^2 \\ S_2 = 2a_1 a_2 \cos \sigma \\ S_3 = 2a_1 a_2 \sin \sigma \end{cases} \tag{12}$$

It is obvious that the Stokes parameters can be derived if the x and y components are clearly represented, and vice versa. Based on the obtained parameters, polarization detection can be verified through orientation angles for LP light and chiral amplitude contrast for arbitrarily polarized light. When σ is set to 0, the light is LP light with an orientation angle of $\arctan\left(\frac{a_2}{a_1}\right)$. When a_1 is identical to a_2, the chiral amplitude contrast of arbitrarily polarized light is only determined by σ. The results and analysis are investigated in Section 3.

B. The refractive index of the material in the simulation based on the fabrication process

Table 1. Refractive index of amorphous silicon used in the simulation

Wavelength	Refractive index	Wavelength	Refractive index
1210	3.514	1384	3.484
1216	3.513	1390	3.484
1222	3.512	1396	3.483
1228	3.511	1402	3.482

Optics EXPRESS

1234	3.510	1408	3.481
1240	3.508	1414	3.480
1246	3.507	1420	3.479
1252	3.506	1426	3.479
1258	3.505	1432	3.478
1264	3.504	1438	3.477
1270	3.503	1444	3.476
1276	3.502	1450	3.476
1282	3.500	1456	3.475
1288	3.499	1462	3.474
1294	3.498	1468	3.473
1300	3.497	1474	3.473
1306	**3.496**	1480	3.472
1312	**3.495**	1486	3.471
1318	3.494	1492	3.471
1324	3.493	1498	3.470
1330	3.492	1504	3.469
1336	3.492	1510	3.469
1342	3.491	1516	3.468
1348	3.490	1522	3.467
1354	3.489	1528	3.467
1360	3.488	1534	3.466
1366	3.487	1540	3.465
1372	3.486	1546	3.465
1378	3.485	1552	3.464

C. Potential fabrication process

The fabrication of a fiber-tip meta-device requires additional steps compared to the conventional metasurface fabrication, namely the preprocessing of the fiber. The preprocessing step starts by striping the coating of one end of the fiber and putting a specially-designed casing on this fiber section subsequently. The length of the casing is (6.5 ∓ 0.5) *mm* and the diameter is (1.8 ∓ 0.005) *mm*. The casing is utilized to fix up the fiber tightly for further fabrication. As shown in Fig. 9, there is a bevel at the end of the casing for buffering. The remaining section outside the casing will be protected by 353ND epoxy and the protective gel to prevent impurities from contacting the fiber during the deposition process.

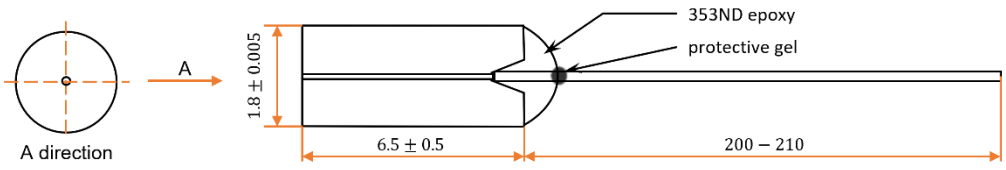

Fig. 9. Schematic demonstration of the preprocessing of the fiber. (The unit of length is a millimeter.)

Optics EXPRESS

The fiber tip will be polished by fine-grinding discs Aka-Piatto to obtain a smooth surface. Afterward, around 60 preprocessed fiber sections will be neatly fixed together for fiber-tip deposition. A thin layer of Aluminum oxide (Al_2O_3), acting as the adhesive, will be first deposited on the fiber tip using the Magnetron Sputtering Coater. As experiments suggested, a directly deposited layer of Amorphous Silicon (a-Si) without the adhesive will be fragile. Besides, the thickness of Al_2O_3 is around 25 nm, which is almost negligible to the designed meta-device. The following deposition of an a-Si layer with 800 nm thickness will be conducted by Low-pressure chemical vapor deposition (LPCVD). There exists a problem that some of the deposited material might fall into the periodic air holes. However, based on previous research on nano structures integrated on LMA-PCF [7,29], the amount of the fallen material is slight and would barely affect the endless single-mode characteristic of the fiber and the defect is considered approximately negligible. Assisted with the specially-designed casing, the nanostructures will be subsequently fabricated using the matched focused ion beam (FIB) system.

D. Detection deviation of 20 polarization states

Table 2. Detection deviation rate for 20 test samples with different states of polarization (%)

Test number	S_1	S_2	S_3	Average deviation
1	2.82	5.39	0.97	3.06
2	6.58	5.97	1.10	4.55
3	1.39	0.15	3.42	1.65
4	6.65	5.37	3.23	5.08
5	3.85	2.20	0.79	2.28
6	5.35	1.05	1.10	2.50
7	2.61	2.19	3.87	2.89
8	3.32	3.18	3.95	3.49
9	6.88	4.75	3.73	5.12
10	0.14	3.00	2.35	1.83
11	7.24	0.68	3.83	3.92
12	2.51	0.30	0.06	0.96
13	8.13	0.66	0.46	3.08
14	2.51	0.30	0.06	0.96
15	3.37	1.05	2.78	2.40
16	2.77	1.99	3.57	2.78
17	4.49	3.06	2.31	3.29
18	0.17	5.69	0.28	2.05
19	1.43	1.18	2.67	1.76
20	4.63	1.44	3.56	3.21
Average deviation	3.84	2.48	2.20	2.84

Funding. National Key Research and Development Program of China (2018YFB1800902); Key Basic Research Scheme of Shenzhen Natural Science Foundation (JCYJ20200109142010888).

Disclosures. The authors declare no conflicts of interest.

Data availability. Data underlying the results presented in this paper are available from the corresponding authors upon reasonable request.

Optics EXPRESS

References

1. M. L. Tseng, M. Semmlinger, M. Zhang, C. Arndt, T. T. Huang, J. Yang, H. Y. Kuo, V. Su, M. K. Chen, C. H. Chu, B. Cerjan, D. P. Tsai, P. Nordlander, and N. J. Halas, "Vacuum ultraviolet nonlinear metalens," Sci. Adv. **8**(16), eabn5644 (2022).
2. S. Wang, S. Wen, Z. Deng, X. Li, and Y. Yang, "Metasurface-Based Solid Poincaré Sphere Polarizer," Phys. Rev. Lett. **130**(12), 123801 (2023).
3. H. Pahlevaninezhad, M. Khorasaninejad, Y. W. Huang, Z. Shi, L. P. Hariri, D. C. Adams, V. Ding, A. Zhu, C. W. Qiu, F. Capasso, and M. J. Suter, "Nano-optic endoscope for high-resolution optical coherence tomography in vivo," Nat. Photonics **12**(9), 540–547 (2018).
4. H. Zhang, X. Sha, Q. Chen, J. Cheng, Z. Ji, Q. Song, S. Yu, and S. Xiao, "All-Dielectric Metasurface-Enabled Multiple Vortex Emissions," Adv. Mater. **34**(14), 2109255 (2022).
5. H. Li, J. T. Kim, J. S. Kim, D. Y. Choi, and S. S. Lee, "Metasurface-Incorporated Optofluidic Refractive Index Sensing for Identification of Liquid Chemicals through Vision Intelligence," ACS Photonics **10**(3), 780–789 (2023).
6. Q. Zhao, W. Yuan, J. Qu, Z. Cheng, G. D. Peng, and C. Yu, "Optical Fiber-Integrated Metasurfaces: An Emerging Platform for Multiple Optical Applications," Nanomaterials **12**(5), 793 (2022).
7. J. Yang, I. Ghimire, P. C. Wu, S. Gurung, C. Arndt, D. P. Tsai, and H. W. Lee, "Photonic crystal fiber metalens," Nanophotonics **8**(3), 443–449 (2019).
8. M. Zeisberger, H. Schneidewind, U. Hübner, T. Wieduwilt, M. Plidschun, and M. A. Schmidt, "Plasmonic metalens-enhanced single-mode fibers: a pathway toward remote light focusing," Adv. Photonics Res. **2**(11), 2100100 (2021).
9. H. Ren, J. Jang, C. Li, A. Aigner, M. Plidschun, J. Kim, J. Rho, M. A. Schmidt, and S. A. Maier, "An achromatic metafiber for focusing and imaging across the entire telecommunication range," Nat. Commun. **13**(1), 4183 (2022).
10. M. Principe, M. Consales, A. Micco, A. Crescitelli, G. Castaldi, E. Esposito, V. L. Ferrara, S. Cutolo, V. Galdi, and A. Cusano, "Optical fiber meta-tips," Light: Sci. Appl. **6**(3), e16226 (2016).
11. C. Zhou, W. B. Lee, S. Gao, H. Li, C. S. Park, D. Y. Choi, and S. S. Lee, "All-Dielectric Fiber Meta-Tip Enabling Vortex Generation and Beam Collimation for Optical Interconnect," Laser Photonics Rev. **15**(5), 2000581 (2021).
12. M. Consales, G. Quero, S. Spaziani, M. Principe, A. Micco, V. Galdi, A. Cutolo, and A. Cusano, "Metasurface-Enhanced Lab-on-Fiber Biosensors," Laser Photonics Rev. **14**(12), 2000180 (2020).
13. T. Martins, Y. Cui, B. Gholipour, J. Y. Ou, O. Frazão, and K. F. MacDonald, "Fiber-Integrated Phase Change Metasurfaces with Switchable Group Delay Dispersion," Adv. Opt. Mater. **9**(21), 2100803 (2021).
14. H. G. Berry, G. Gabrielse, and A. E. Livingston, "Measurement of the Stokes parameters of light," Appl. Opt. **16**(12), 3200–3205 (1977).
15. G. Cao, H. X. Xu, L. M. Zhou, Y. Deng, Y. Zeng, S. Dong, Q. Zhang, Y. Li, H. Yang, Q. Song, X. Liu, Y. Li, and C. W. Qiu, "Infrared metasurface-enabled compact polarization nanodevices," Materials **50**, 499–515 (2021).
16. Y. Cao, L. Tang, R. Jin, J. Li, J. Wang, and Z. Dong, "Grayscale image for broadband linear polarization measurement by an ultracompact metasurface," Opt. Lett. **46**(5), 1117–1120 (2021).
17. S. Tian, H. Guo, J. Hu, and S. Zhuang, "Dielectric longitudinal bifocal metalens with adjustable intensity and high focusing efficiency," Opt. Express **27**(2), 680–688 (2019).
18. J. Wei, Y. Chen, Y. Li, W. Li, J. Xie, C. Lee, K. S. Novoselov, and C. W. Qiu, "Geometric filterless photodetectors for mid-infrared spin light," Nat. Photonics **17**(2), 171–178 (2023).
19. A. Ma, Y. Intaravanne, J. Han, R. Wang, and X. Chen, "Polarization Detection Using Light's Orbital Angular Momentum," Adv. Opt. Mater. **8**(18), 2000484 (2020).
20. E. Arbabi, S. M. Kamali, A. Arbabi, and A. Faraon, "Full-Stokes Imaging Polarimetry Using Dielectric Metasurfaces," ACS Photonics **5**(8), 3132–3140 (2018).
21. P. C. Wu, J. W. Chen, C. W. Yin, Y. C. Lai, T. L. Chung, C. Y. Liao, B. H. Chen, K. W. Lee, C. J. Chuang, C. M. Wang, and D. P. Tsai, "Visible Metasurfaces for On-Chip Polarimetry," ACS Photonics **5**(7), 2568–2573 (2017).
22. J. Bai, C. Wang, X. Chen, A. Basiri, C. Wang, Y. Yao, A. Pors, M. G. Nielsen, and S. I. Bozhevolnyi, "Chip-integrated plasmonic flat optics for mid-infrared full-Stokes polarization detection," Photonics Res. **7**(9), 1051–1060 (2019).
23. A. Basiri, X. Chen, J. Bai, P. Amrollahi, J. Carpenter, A. Holman, C. Wang, and Y. Yao, "Nature-inspired chiral metasurfaces for circular polarization detection and full-Stokes polarimetric measurements," Light: Sci. Appl. **8**(1), 78 (2019).
24. A. Pors, M. G. Nielsen, and S. I. Bozhevolnyi, "Plasmonic metagratings for simultaneous determination of Stokes parameters," Optica **2**(8), 716–723 (2015).
25. S. Zhang, S. Yang, W. Yue, Q. Xu, C. Tian, X. Zhang, E. Plum, S. Zhang, J. Han, and W. Zhang, "Direct polarization measurement using a multiplexed Pancharatnam–Berry metahologram," Optica **6**(9), 1190–1198 (2019).
26. J. P. Balthasar Mueller, K. Leosson, and F. Capasso, "Ultracompact metasurface in-line polarimeter," Optica **3**(1), 42–47 (2016).
27. N. A. Rubin, G. D'Aversa, P. Chevalier, Z. Shi, W. T. Chen, and F. Capasso, "Matrix Fourier optics enables a compact full-Stokes polarization camera," Science **365**(6448), eaax1839 (2019).
28. Y. D. Shah, A. S. Dada, J. P Grant, D. R. S. Cumming, C. Altuzarra, T. S. Nowack, A. Lyons, M. Clerici, and D. Faccio, "An all-dielectric metasurface polarimeter," ACS Photonics **9**(10), 3245–3252 (2022).
29. I. Ghimire, J. Yang, S. Gurung, S. K. Mishra, and H. W. H. Lee, "Polarization-dependent photonic crystal fiber optical filters enabled by asymmetric metasurfaces," Nanophotonics **11**(11), 2711–2717 (2022).